Advanced Functional Materials

ADVANCED FUNCTIONAL MATERIALS
www.afm-journal.de

RESEARCH ARTICLE OPEN ACCESS

Bio-Orthogonally Crosslinked Supramolecular Polymer Bottlebrush Hydrogels for Long-Term 3D Cell Culture

Ceren C. Pihlamagi[1,2] | David Pretzel[1,2] | Peer Nölte[4] | Kourosh Rezaei[3] | Ulrich S. Schubert[1,2] | Johannes C. Brendel[4,5]

[1]Laboratory of Organic and Macromolecular Chemistry (IOMC), Friedrich Schiller University Jena, Jena, Germany | [2]Jena Center for Soft Matter (JCSM), Friedrich Schiller University Jena, Jena, Germany | [3]Linkdlab GmbH, Jena, Germany | [4]Macromolecular Chemistry, University of Bayreuth, Bayreuth, Germany | [5]Institute of Macromolecular Research (BIMF) and Bavarian Polymer Institute (BPI), University of Bayreuth, Bayreuth, Germany

Correspondence: Johannes C. Brendel (johannes.brendel@uni-bayreuth.de)

Received: 27 August 2025 | **Revised:** 13 December 2025 | **Accepted:** 8 January 2026

Keywords: 3D cell culture | fibrous scaffolds | hydrogel materials | self-assembly | SPAAC crosslinking | supramolecular polymer bottlebrushes

ABSTRACT

The native extracellular matrix (ECM) comprises fibrous networks formed by supramolecular assembly of biomacromolecules, which provides cells mechanical support and bioactive cues. As synthetic mimics of ECM, hydrogels made of supramolecular motifs are prospective candidates resembling the fibrous nature of ECM and providing a versatile platform for further functionalization. As recently reported, poly(ethylene oxide) (PEO) modified benzenetrispeptide (BTP) motifs can self-assemble into supramolecular bottlebrush-like fibers and form biocompatible hydrogels when crosslinked. However, previous gelation methods are not suitable for 3D cell encapsulation. Herein, we introduce a bio-orthogonal, strain-promoted azide-alkyne cycloaddition (SPAAC) crosslinking strategy enabling a fast and selective coupling under cell-compatible conditions. The properties of the hydrogels can be tuned by fiber and crosslinking concentrations. Importantly, our design approach enables long-term (up to 10 days) 3D cell culture, although the system is intrinsically bioinert. Deep-learning-assisted image analysis reveals that the fiber content significantly influences cell viability and colony growth across multiple cell lines. Long-term live cell imaging indicates that colony formation occurs by division of single cells rather than the pre-gelation aggregation of individual cells. As a step toward employing BTP hydrogels as ECM mimics, these findings underscore the role of supramolecular design in directing the formation pathways of multicellular assemblies.

1 | Introduction

Mimicking extracellular matrix (ECM) has become a widely adopted strategy in biomedical applications such as tissue engineering and bio-electronics [1–5]. Natural ECM-derived materials (e.g., decellularized ECMs and collagen) can support cell encapsulation and growth but often suffer from batch-to-batch variation limiting their clinical transitions [6]. On the other hand, synthetic hydrogels offer well-defined, tunable, and scalable platforms with improved reproducibility.

Early generations of synthetic hydrogels based on covalently crosslinked polymers, including poly(ethylene glycol) (PEG), poly(*N*-isopropylacrylamide) (PNIPAM), and polyurethanes, provided advantages in reproducibility and mechanical tunability [1, 3]. One limitation is the potential immunogenicity of these polymers and the toxicity of residual monomers [7, 8]. Furthermore, these 3D polymer networks fail to reflect the dynamic and fibrous characteristics of the native extracellular matrix (ECM), which are critical for regulating cellular behavior [9–12]. To address this limitation, strategies including the incorporation of dynamic

covalent crosslinking, biodegradable motifs, or controlled porosity have been introduced to enhance the biological performance [1, 13–15].

In parallel, supramolecular hydrogels have emerged as next-generation ECM mimics with distinct advantages. Systems relying on peptide amphiphiles (PA), benzene-1,3,5-tricarboxamide (BTA), or ureido-pyrimidinone (UPy) motifs have been extensively investigated as ECM mimics [16]. These motifs self-assemble into fibrous networks demonstrating tunable mechanical and biological performance through molecular design, crosslinking control, and incorporation of bioactive cues. The non-covalent, supramolecular nature of these systems imparts adaptive behavior and confers viscoelastic properties to the resulting materials [17]. Nevertheless, most supramolecular hydrogels reported to date rely on reversible or dynamic self-assembly processes, which frequently compromise the structural stability of the fibers [16, 18, 19]. Consequently, these systems are susceptible to disintegration upon dilution or when exposed to complex biological environments, particularly over prolonged time frames. Furthermore, the incorporation of bulky biofunctional units into the assembly motifs can exacerbate disruption of the self-assembly process.

Here, we present supramolecular polymer bottlebrush (SPB) hydrogels as 3D cell scaffolds that resemble the stability and functionality of conventional covalent polymer hydrogels, but still feature a fibrous nature and viscoelastic properties known for supramolecular systems. The system relies on previously reported polyethylene oxide (PEO) modified benzenetrispeptide (BTP) motifs, which self-assemble into bottlebrush-like supramolecular fibers via kinetically controlled pathways [20–22]. In contrast to previous attempts to create hydrogels requiring organic solvents [23, 24], we here developed an approach in which BTP-based fibers are post-assembly connected through bio-orthogonal, copper-free strain-promoted azide-alkyne cycloaddition (SPAAC) crosslinking under cell compatible conditions (Figure 1) [25, 26]. In contrast to other strategies, reinforcing supramolecular assemblies with covalent crosslinking, as for example explored by Baker et al. [27] and Pal and Ghosh et al. [28], our work introduces a complementary concept achieving structural stabilization of SPB fibers under physiological conditions while preserving the intrinsic noncovalent character of the supramolecular fibers and the viscoelastic properties of the resulting network. To the best of our knowledge, such a SPAAC-induced crosslinking strategy in the presence of cells has previously been utilized only in 3D polymer networks [26] and collagen-based natural systems to enhance the mechanical robustness [29, 30]. Unlike other supramolecular fibrous hydrogels [31–33], which rely on gelation by dynamic exchange processes, pH change, and thermoresponsive behavior, the current method provides a chemically defined and versatile platform for systematically investigating how fibrous microenvironments regulate cell behavior.

With this motivation, we prepared BTP hydrogels by varying the fiber content (1.2–2.5 wt%) and crosslinker (CL) concentration (5–20 mol%) and investigated the rheological behavior of the resulted hydrogel formulations. To reveal the applicability of BTP hydrogels for 3D cell culture, we encapsulated different cell lines; L929 fibroblasts cells, MCF-7 and MDA-MB-231 cancer cells, and MDCK kidney epithelial cells. We studied the effect of fiber content on cell viability and colony growth over 10 days by utilizing fluorescein diacetate/propidium iodide (FDA/PI) staining-based live/dead cell analysis. Moreover, we implemented deep-learning-assisted image processing to quantify live/dead cell populations and the area of multicellular assemblies in a high-throughput way. We further tracked the pathway of colony formation via live cell microscopy.

2 | Results and Discussion

In order to make BTP system suitable for biocompatible cell encapsulation, we prepared a hybrid supramolecular fiber made of BTP-PEO and BTP-PEO-N_3 motifs via solvent switching method (Figure 1). The reason for aiming at a hybrid system is that fibers formed exclusively from the BTP-PEO-N_3 motif had the tendency to spontaneously gel upon solvent evaporation, indicating additional interfiber interactions compared to pure BTP-PEO system (Figure S2a). We have previously observed that subtle changes in the assembly can have an effect on the final rheological properties of concentrated systems, which we attribute to differences in the entanglement of the fibers. As we decreased the molar ratio of BTP-PEO-N_3 motif, we observed a reduction in fiber solution viscosity. Considering the processability of the system for homogenous crosslinking and cell encapsulation, we selected a hybrid formulation containing 20 mol% BTP-PEO-N_3 motif. Upon addition of CL, PEG_{10kDa} end-capped with dibenzocyclooctyne, and incubation the system at 37°C for 40 min, the hydrogel forms (Figure S2b). Moreover, the selected system enabled homogeneous encapsulation of L929 cells in the hydrogel matrix without formation of local cell aggregates (Figure S2c).

Due to the novelty of our system, it is important to identify a tunable formulation range that supports long-term cell viability and growth. Therefore, we selected a fixed crosslinking concentration (10 mol%) and systematically varied the fiber content (1.2, 1.5, 2.0, and 2.5 wt%) based on preliminary optimization for extended 3D cell culture (Figures S2d and S3, Table S1). This approach enabled us to isolate the effect of fiber concentration on gel stiffness, which is a key parameter for designing materials that mimic native ECM [16, 34]. Formulations below 1.1 wt% did not form intact hydrogels, and the 1.1 wt% composition gradually lost integrity during the long-term culture process. For this reason, lower concentrations were excluded from further investigations. For the rheological characterization of the hydrogels, we first performed amplitude sweep measurements for two extreme fiber concentrations (2.5 and 1.2 wt%) to determine the linear viscoelastic region of the hydrogels (Figure S4). The complex shear strain was changed from 0.1 to 100% at a constant frequency of 1 Hz. With increasing CL content, the storage modulus (G′) of the hydrogels increased, and the crossover between G′ and the loss modulus (G″) shifted to lower strain. This behavior is consistent with a denser supramolecular fiber network, indicating more transient junctions and greater entanglement. A complex shear strain of 0.5% was selected for all subsequent rheological measurements because it falls within the linear viscoelastic region for all tested formulations and minimizes the risk of network disruption during testing.

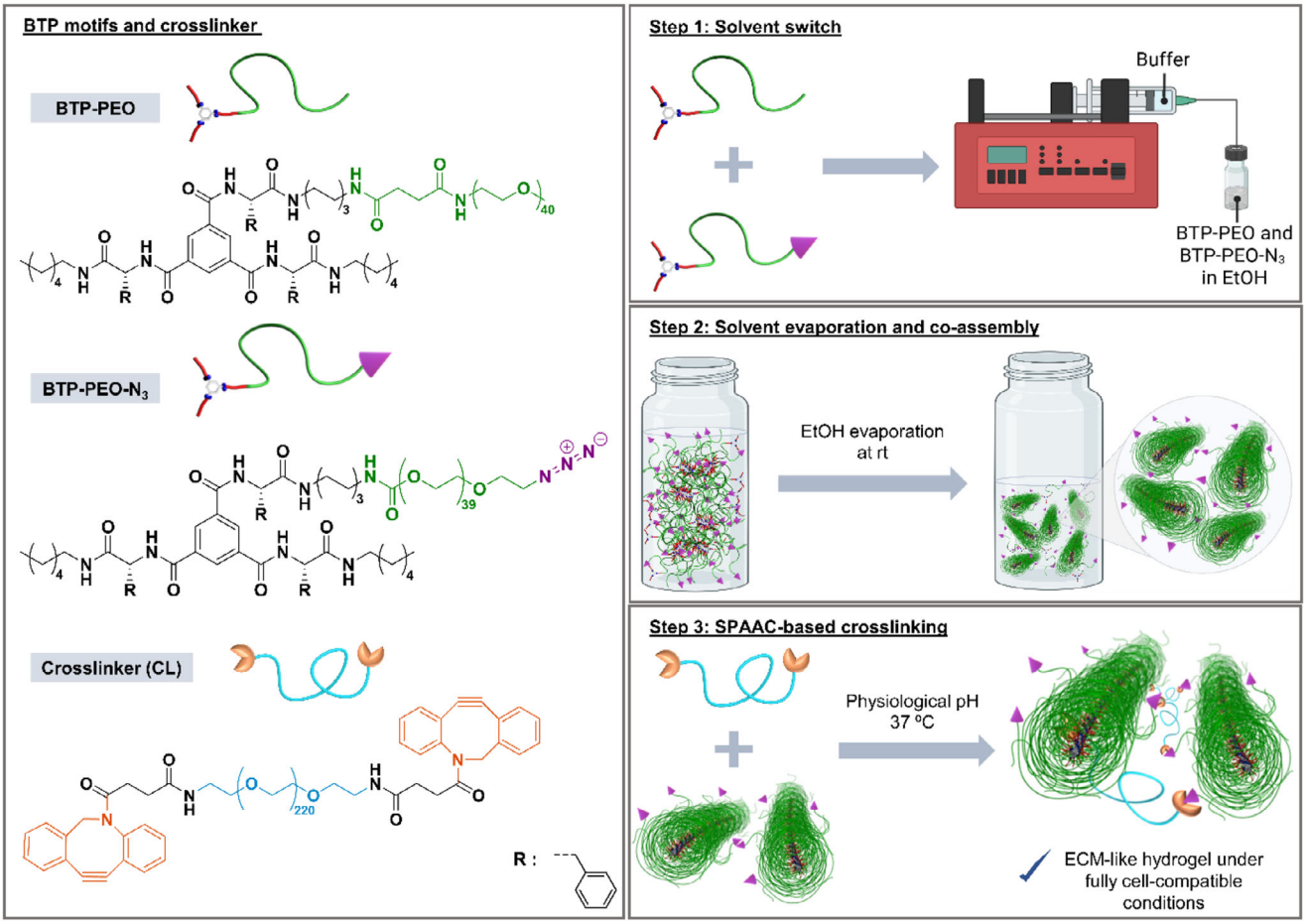

FIGURE 1 | Schematic illustration of cell-compatible hydrogel formation. BTP-PEO and BTP-PEO-N_3 motifs assemble into hybrid supramolecular fibers that are further stabilized by the covalent crosslinking via SPAAC while preserving the noncovalent character of the network.

To investigate the influence of fiber concentration on the mechanical properties of hydrogel networks, frequency sweep tests were performed across a range of 0.1–100 Hz (Figure 2a; Figures S5 and S6). This analysis provided insight into the viscoelastic behavior of the hydrogels across a range of deformation rates. For all formulations, G′ was higher than G″, confirming the formation of stable hydrogel networks with a broad range of fiber and crosslinking contents. At a constant crosslinking ratio, decreasing the fiber concentration from 2.5 to 1.2 wt% resulted in a clear reduction in G′ values [35]. A similar trend in G′ values was also observed when the crosslinker content decreases from 20 to 2.5 mol% at a fixed fiber content [36]. Although the current system shows lower absolute G′ values (from ~760 to ~104 Pa) (Table S2) compared to our previous BTP-based hydrogels, both hydrogel systems follow the same trend of decrease in stiffness with reduced fiber and crosslinking concentration [24]. The system-dependent variations in G′ values may arise from the differences in formulation and/or crosslinking methods that influence fiber organization (entanglement and bundling) and, consequently, the mechanical properties [33]. To further test the reversibility of network interactions, step-strain experiments were performed at various fiber concentrations (Figure S7). After each high-strain deformation, the hydrogels rapidly regained their initial G′ and G″ values, confirming that reversible supramolecular junctions persist within the covalently crosslinked framework. The extent of recovery and absolute modulus increased with fiber content, consistent with denser supramolecular reinforcement.

In order to evaluate the gelation kinetics based on SPAAC crosslinking, we performed time sweep measurements. For all formulations, G′ values were instantly higher than G″, indicating a rapid formation of a network structure by the crosslinking reaction (Figure 2b; Figure S8). An initial G′-G″ crossover could not be detected as the SPAAC crosslinking reaction occurs faster than the time required for sample preparation and loading onto the rheometer (~1 min). Initially formed network systems are soft and weak (G′ < 10 Pa), and the development of a stable, self-supporting hydrogel occurs gradually over ~40 min as the network equilibrates. Increasing both fiber and CL contents accelerated the gelation process with a consistent trend across all tested samples. Although reported SPAAC-based gelation times vary among different systems [37], similar secondary strengthening and equilibration periods have been observed in conventional covalent hydrogels [38, 39]. Moreover, azide-modified collagen-based systems exhibited similar moderate gelation kinetics [29, 30].

Although it might be considered detrimental to uniform cell distribution, the observed moderate system stabilization time offers greater flexibility for homogeneous mixing of components, including cells, and allows the integration of complex workflows

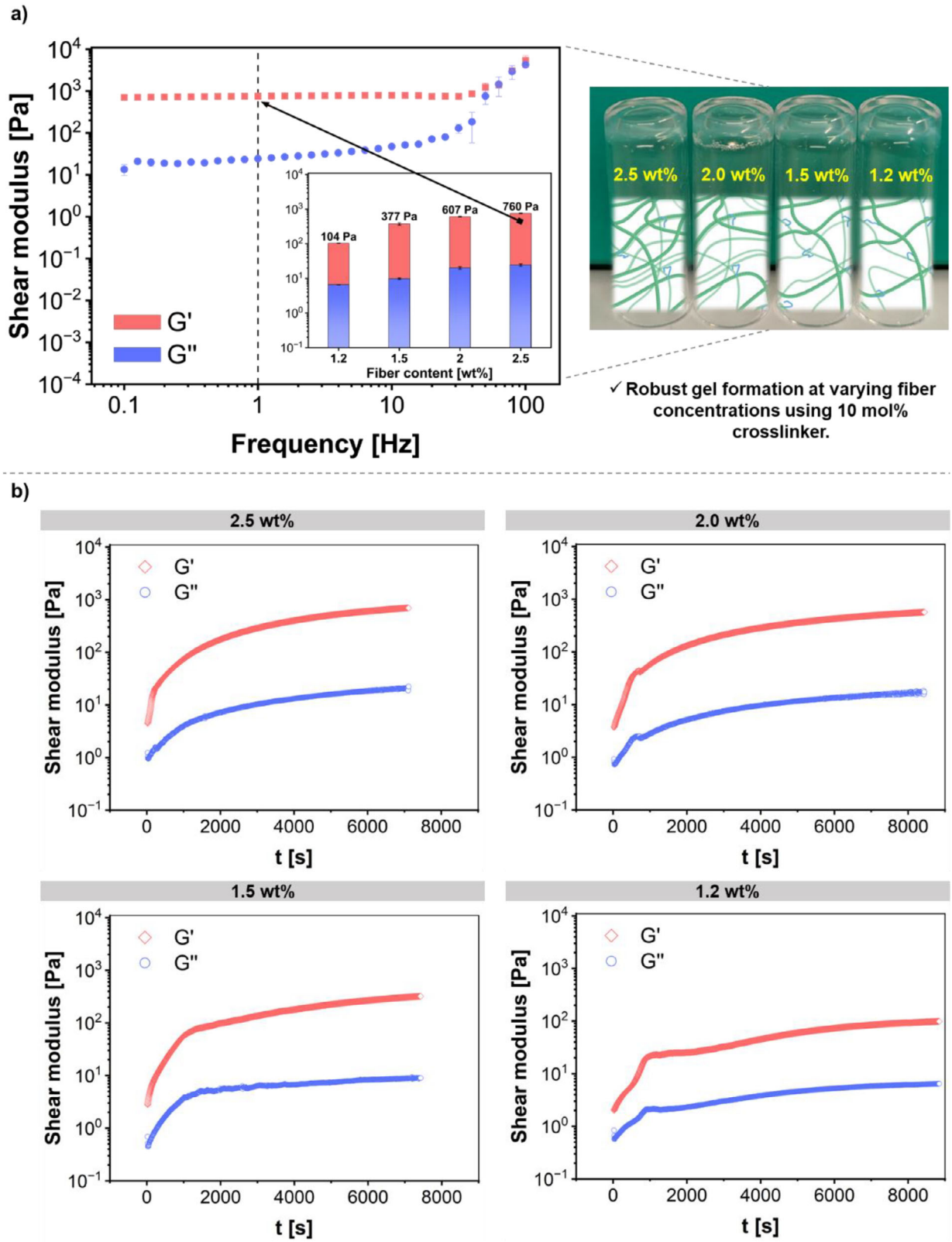

FIGURE 2 | Rheological investigations of hydrogels with 1.2–2.5 wt% fiber and 10 mol% CL contents. (a) Frequency sweep measurements conducted with a complex shear strain of 0.5% and the data are represented as mean ± SD ($n = 3$). The inset bar plot summarizes average G′ and G″ values at 1 Hz. The photograph shows the corresponding hydrogels after gelation. (b) Time sweep measurements to monitor the gelation kinetics starting subsequently to the addition and mixing of the CL. All measurements were conducted at 37°C. For rheological characterizations at varying CL ratios (2.5, 5, and 20 mol%), see Figures S5, S6, and S8.

at room temperature by eliminating the need for rapid mixing protocols or cold chain handling [6, 40]. Moreover, the increased viscosity of the pre-made fiber solutions appears to prevent a premature sedimentation of cells, which again simplifies processing.

For long-term 3D cell culture, it is crucial that hydrogels remain intact during medium addition and exchange throughout the culture period, while efficiently serving as nutrient reservoirs and facilitating waste removal. These requirements can be fulfilled for crosslinked polymer hydrogels, but dynamic supramolecular systems might suffer from continuous swelling and dilution of the system due to long-term dynamic exchange. The presented supramolecular system; however, demonstrates that once the BTP fibers are crosslinked, the hydrogels remain stable during media addition and exchange over 10 days for all tested fiber contents (1.2–2.5 wt%) (Figure S2d). To further demonstrate the structural stability, stress-relaxation rheology experiments were performed before and after 10 days of incubation in cell culture medium at 37°C (Figure S9 and Table S3). Nearly identical stress-relaxation profiles and relaxation half-times across all fiber concentrations were observed confirming that the mechanical integrity and dynamic viscoelastic properties of the hydrogels are maintained under cell culture conditions. Furthermore, phenol red, as a small molecule present in the cell culture medium, was able to completely diffuse through the 2.5 wt% hydrogel without visible swelling, indicating no spatial change or dilution of the network; one of the major concerns for fibrous supramolecular systems (Figure S2e).

To evaluate the potential of our system for 3D cell culture, we examined four different cell lines (L929, MCF-7, MDA-MB-231, and MDCK cells), which were embedded into hydrogel formulations with fiber concentrations ranging from 1.2 to 2.5 wt% with 10 mol% CL in predetermined time periods (day 2, 6, and 10) (Figure 3a). The viability and morphology of the cultured cells were determined by a live/dead cell assay based on an Fluorescein Diacetate/Propidium Iodide (FDA/PI) staining assay. PI enters into the nuclei of dead cells due to the loss of cell membrane integrity and interacts with the genetic material to give a red, local fluorescence signal. On the other hand, live cells with an intact cell membrane are detected by a green fluorescence signal, which is a result of the cleavage of FDA upon esterase activity after its internalization. Confocal images obtained after 2 days of incubation revealed that live cells retained a rounded, unattached morphology, consistent with the bioinert nature of the hydrogel system (Figure 3b). Cell viability was strongly influenced by fiber content. At lower fiber concentrations (1.2 and 1.5 wt%), most cell types remain viable by showing the predominance of green fluorescence signal. In contrast, increasing the fiber content to 2.0 and 2.5 wt% led to a progressive reduction in green signal accompanied by an increase in red signal, reflecting the decrease in cell viability. The extent of viability loss differed among the examined cell types.

In addition to the qualitative observations, cell viability was quantitatively assessed by employing deep-learning-based image analysis workflow (Figure S10). For this purpose, we applied an automated image analysis workflow based on the Segment Anything Model (SAM2.1), a recently developed artificial intelligence tool trained to detect and outline objects in images [41]. Subsequently, we performed post-processing and mask classification by utilizing OpenCV [42]. This workflow enabled reliable and unbiased quantification of live/dead events from the confocal images taken after 2 days of culture (Figure 3c; Table S5). Except MDA-MB-231 cells, all cell lines showed a significant decrease in cell viability (< 50%) for 2.0 and 2.5 wt% fiber contents (Table S6). Even though observed bulk stiffness for all tested formulations are in the range of soft hydrogels (< 1 kPa), the increase in fiber content can cause a change in local stiffness and/or degree of fiber entanglement that cells experience in their microenvironments [16]. The higher tolerance of MDA-MB-231 cells to the increase in fiber content may arise from their adaptivity to the variations in local stiffness [43]. Moreover, cytoskeletal plasticity and the invasive phenotype of MDA-MB-231 cells can also promote their survival in mechanically restrictive environments [44]. Further biomechanical investigations are planned in this direction.

Another explanation for the reduction in cell viability with an increase in fiber concentration could be the restriction of the diffusivity of necessary nutrients, oxygen, and metabolites due to densely packed inter-fiber regions. Therefore, we investigated the diffusion coefficients of fluorescein labeled IgG (FITC-IgG, Mw: ~150 kDa, *R*h: 5.6 to 5.9 nm) [45] in hydrogels with the lowest (1.2 wt%) and highest (2.5 wt%) fiber contents with 10 mol% CL by utilizing fluorescence recovery after photobleaching (FRAP) experiments [46, 47]. The mean diffusion coefficients were calculated as (D) as 2.07 ± 0.02 and 1.14 ± 0.07 $\mu m^2\ s^{-1}$ for 1.2 and 2.5 wt% hydrogels, respectively (Figure S11). The similar trends are reported in the literature (1 to 5 $\mu m^2\ s^{-1}$) depending on the mesh size and/or polymer content [48, 49]. Our previous work on PEO-decorated BTU hydrogels revealed already that dense hydrated PEO chains can slow down the diffusion of small to large molecules, but never fully immobilized them [23]. Similarly, IgG as large biomacromolecules remained diffusible in the present system, with a negligible immobile fraction ($\gamma_0 \approx 0$). As IgG is larger than many nutrients and signaling molecules required for cell survival, FRAP results suggest that mass transport cannot be severely hindered because of the fiber content. Thus, diffusion limitations are unlikely to be the primary cause of reduced cell viability at higher fiber contents, whereas the biomechanical factors mentioned above are more likely the major reason for this effect.

In addition to culturing cells in the bulk hydrogel, we further tested cell growth on solid supports covered with the hydrogel to gain more insight into the effect of fiber content, and thus the mechanical restriction on cell attachment (Figure S12). L929 cells were first seeded on tissue culture-treated plates and incubated for 24 h to allow complete cell attachment. Afterwards, on top of the attached cells fiber solutions (1.5 and 2.5 wt%) freshly mixed with 10 mol% CL were added, and the systems were incubated at 37°C under a humidified 5% (v/v) CO_2 atmosphere for 40 min to form hydrogels on top of the attached cells. After gelation, the samples were investigated by inverted light microscopy. Cells underneath of hydrogels appeared rounded, indicating a reversible detachment from the culture plate surface. The possible reason was physical lifting of the cells during the addition of fiber solutions and/or transient delays in nutrient availability during gelation. Following the microscopic investigations, cell culture media were added on top of the hydrogels, and the systems were incubated for 2 days. Bright field images indicated that cells

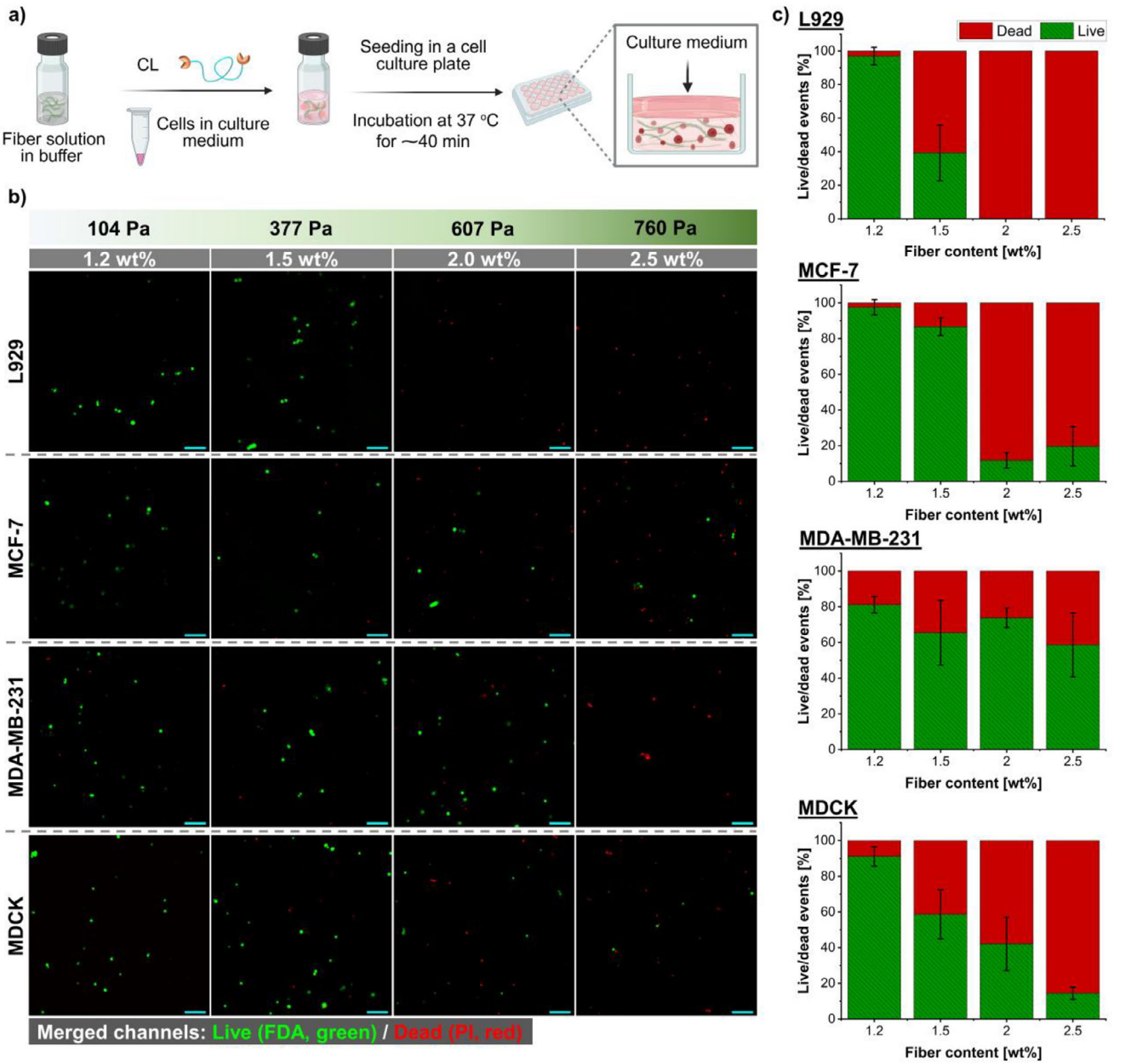

FIGURE 3 | Evaluation of cell viability of L929, MCF-7, MDA-MB-231, and MDCK cells cultured for 2 days in hydrogels with increasing fiber content and 10 mol% CL. (a) Schematic overview of the 3D cell encapsulation workflow. (b) Representative confocal overlay images of live (green, FDA) and dead (red, PI) cells for each formulation. The storage modulus (G′) corresponding to each fiber content is indicated above the images. Scale bars = 100 μm. The images were taken from three randomly selected fields of view per sample ($n = 3$). (c) Quantification of live (green) and dead (red) events via a deep-learning-based segmentation workflow on confocal images.

under 1.5 wt% hydrogels re-attached on the culture plate within 2 days. In contrast, cells under 2.5 wt% hydrogels mostly remained rounded, showing a restriction in cell elongation and attachment in the denser fiber network. These results support that increasing fiber density imposes mechanical constraints on cells rather than severely limiting nutrient diffusion.

For the cell survival in 3D scaffolds, cells should either attach to the bioactive cues in the system or create cell–cell interactions [16]. Particularly, the critical role of bioactive cues in sustaining long-term cell viability in hydrogels has been well documented [33, 50–53]. Since our system is bioinert and no sign of attachment was observed, we tested how far the difference in fiber content can support cells without adhesion. For this purpose, we incubated cells in our 3D systems for up to 10 days. The hydrogels with 2.0 and 2.5 wt% fiber contents did not support the formation of multicellular communities, and most cells progressively lost their viability (Figure S13 and Table S4). In contrast, cells in hydrogels with 1.2 and 1.5 wt% fiber contents remained mostly viable and formed multicellular assemblies over time (Figure 4). These findings additionally support our earlier argument that changes in the microenvironment of cells can explain the fiber content-dependent cell viability. Lower fiber concentrations (1.2 and 1.5 wt%) accordingly provide greater spatial freedom and allow

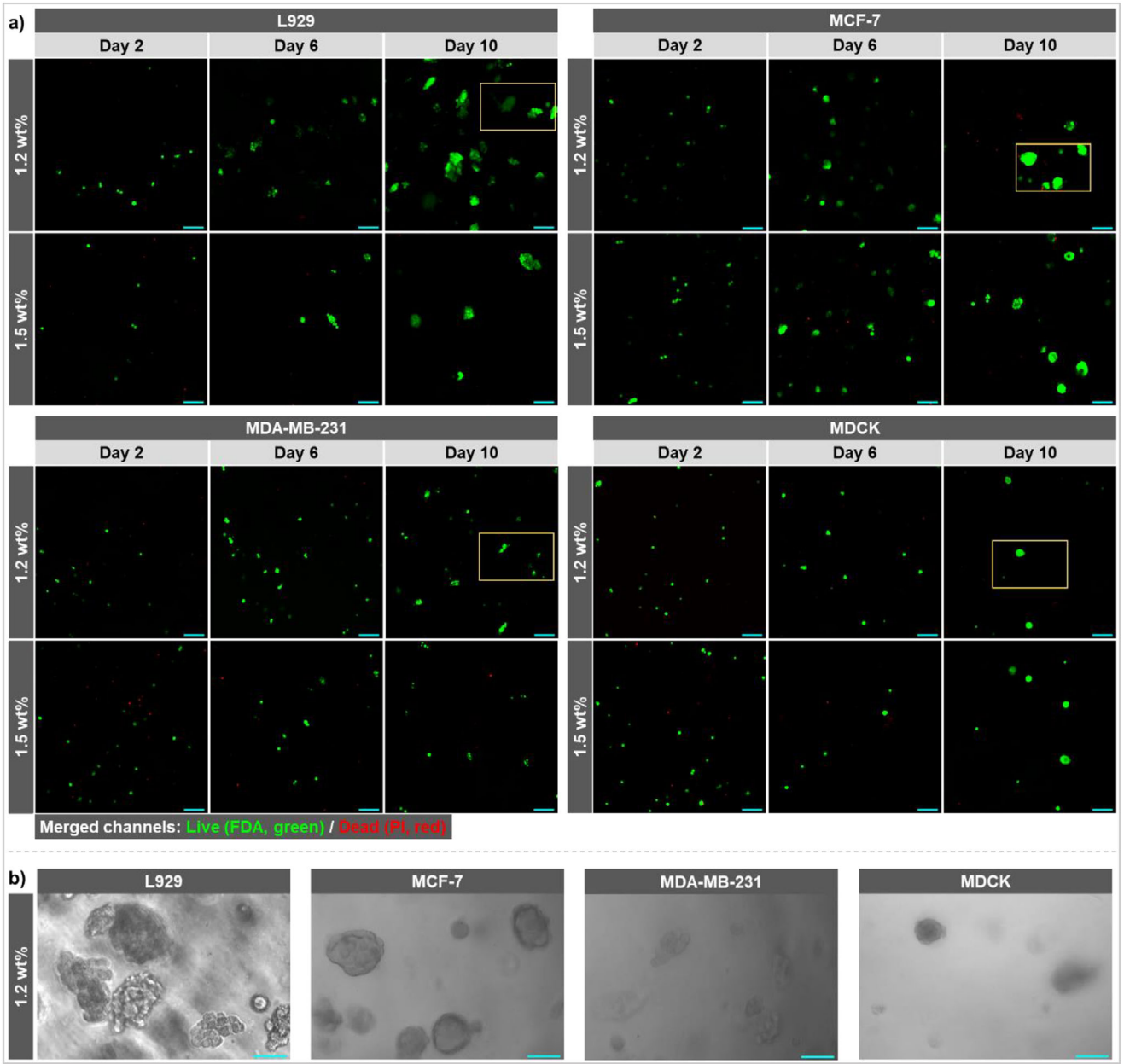

FIGURE 4 | (a) Representative confocal overlay images of live (green, FDA) and dead (red, PI) cells cultured for days 2, 6, and 10 in hydrogels with 1.2 and 1.5 wt% fiber content and 10 mol% CL. The images were taken from three randomly selected fields of view per sample ($n = 3$). Yellow boxes indicate exemplarily chosen colonies for bright-field images shown in (b). Scale bars = 100 μm. (b) Bright-field images of representative colonies after 10 days of culture in 1.2 wt% hydrogels. Scale bars = 50 μm.

better local matrix deformation, which facilitates cell survival and expansion. Consistent with this, combined step-strain and stress-relaxation measurements (Figures S7 and S9, Table S3) revealed that the lower-fiber-content hydrogels (1.2 and 1.5 wt%) recover more rapidly and dissipate stress faster, providing greater local mechanical adaptability and thus enhance the cellular deformation and colony formation. This relationship aligns with previous studies emphasizing the role of viscoelastic relaxation in promoting cellular remodeling and survival in synthetic matrices [54, 55]. By day 10, colony growth occurred for all cell lines through cell–cell interactions due to the absence of biochemical adhesion cues. L929 and MCF-7 cells formed bigger colonies in comparison to MDA-MB-231 and MDCK cells. For larger colonies, the impact of fiber content on colony size was more pronounced. MCF-7 and MDCK epithelial cell colonies exhibited compact morphologies, whereas L929 fibroblasts and MDA-MB-231 cells with mesenchymal-like phenotype developed more elongated colonies (Figure S14). The observed morphological differences among cell lines may reflect intrinsic phenotypic traits. Because fibroblasts and mesenchymal cells possess minimal or no E-cadherin, their cell–cell interactions are limited, and they tend to be more motile [56–58]. In contrast, epithelial cells generally remain stationary and form compact cell–cell aggregates due to the presence of E-cadherin [59, 60].

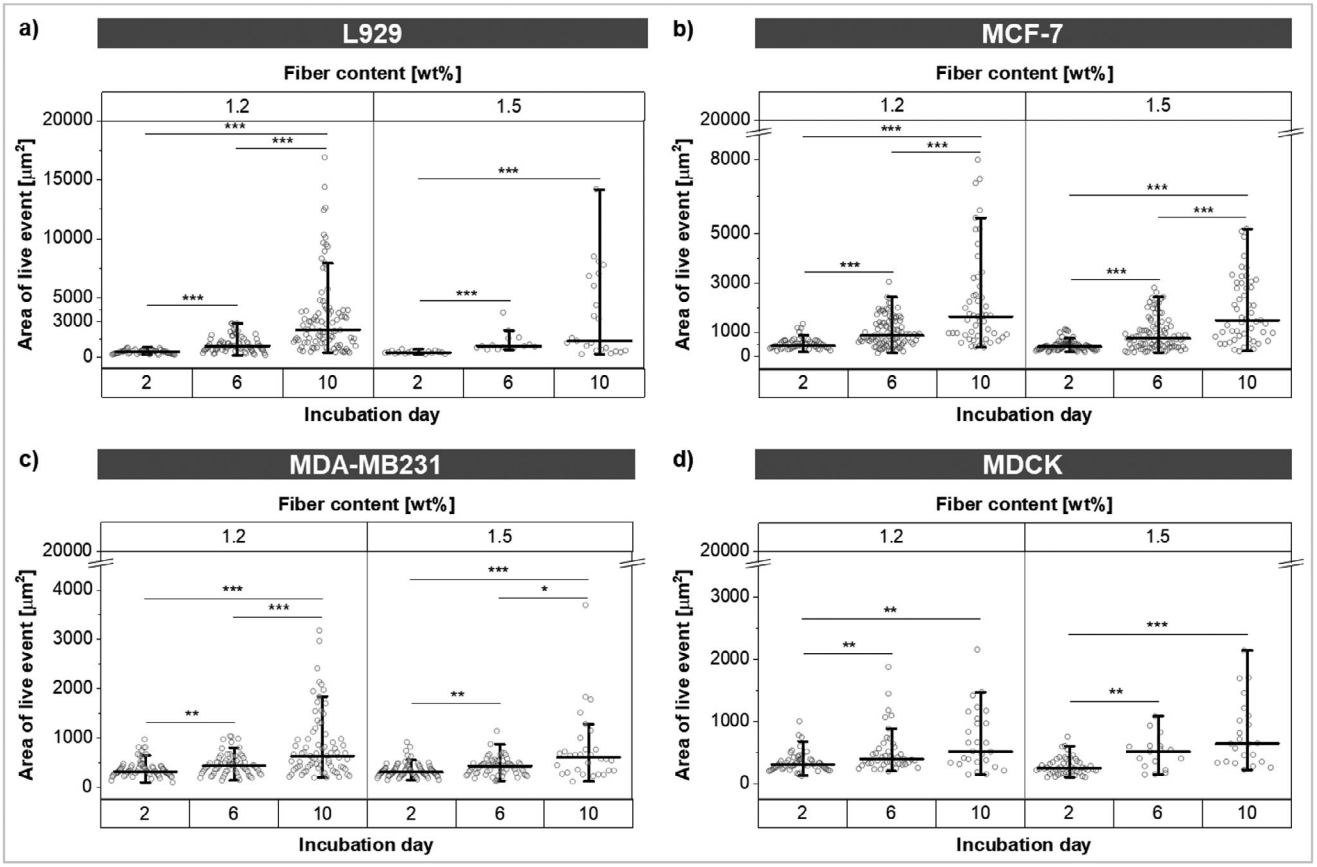

FIGURE 5 | Quantification of the area of live events for (a) L929, (b) MCF-7, (c) MDA-MB-231, and d) MDCK cells cultured in hydrogels with two fiber contents (1.2 and 1.5 wt%) and 10 mol% CL over a 10-day period. Data represent individual live events identified from the deep-learning workflow based on confocal images ($n = 3$). Horizontal bars indicate median values, and whiskers show ± SD. Statistical comparisons were performed as described in the Experimental Section, with significance shown as *, $p < 0.05$; **, $p < 0.01$; ***, $p < 0.001$.

To quantitatively examine the impact of fiber content on colony growth, the area of green events was determined by our deep-learning workflow. The corresponding scatter plots (Figure 5) include all observed colonies, which are plotted according to the individual colony size (connected green area) except outliers. The obtained data were further analyzed to reveal statistical significance. Overall, we observed a progressive increase in the median area of live events from day 2 to 10 (Table S6). At day 10, all four cell lines exhibited a significant increase in colony size, yet the extend of growth was dependent on both fiber content and cell type. On day 10, most of the colonies were larger in the hydrogel with 1.2 wt% fiber content compared to the gels with 1.5wt%, which indicates a greater matrix restriction at higher fiber density. L929 cells exhibited the largest increase in colony area over time, which may result from a higher proliferation rate and/or more pronounced ability to deform the surrounding network. MCF-7 cells displayed a comparable colony growth to L929 cells. MDA-MB-231 and MDCK cells exhibited slower colony growth but followed a similar trend to that observed for L929 and MCF-7 cells. These differences cannot be readily explained by proliferation rates alone, as our system may enforce as-yet unknown restrictions on cell growth, and direct comparisons of fibroblast (L929), epithelial (MCF-7, MDCK), and mesenchymal-like (MDA-MB-231) cell growth in bioinert hydrogels are scarce. Moreover, our system does not resemble 2D monolayer models, where there are restricted cell–cell interactions and unlimited access to nutrients, oxygen, and metabolites [61]. Nonetheless, we can speculate that variations in cell-matrix interactions in combination with intrinsic cell phenotypes may lead to the observed growth and morphological differences; a hypothesis which will be addressed in future studies.

In unmodified bioinert hydrogels, cell–cell interactions are the main driving force for cell survival and multicellular colony formation. Previous studies have shown that traditional 3D polymer networks alone cannot support the formation of multicellular aggregates [62–64]. For supramolecular hydrogels, cell-encapsulation studies have mostly been conducted in systems containing bioactive cues [33, 65–67]. In regard of bioinert fibrous systems, a recent study on BTA motifs demonstrated that controlling network dynamics in the hydrogel enables ATDC5 cells and human mesenchymal stem cells to form multicellular communities through cell aggregation due to dynamic reorganization of the supramolecular assemblies [31]. However, our BTP system does not resemble common polymer networks nor does it involve the dynamic exchange of building blocks [23, 68]. Nevertheless, transient stress relaxation may still arise from reversible disruption of supramolecular crosslinks [69], partial fiber dissociation, or limited rearrangement of the BTP–PEO junctions [70]. These mechanisms are likely to govern the typical viscoelastic behavior of supramolecular bottlebrush networks and may contribute to their favorable mechanical adaptability

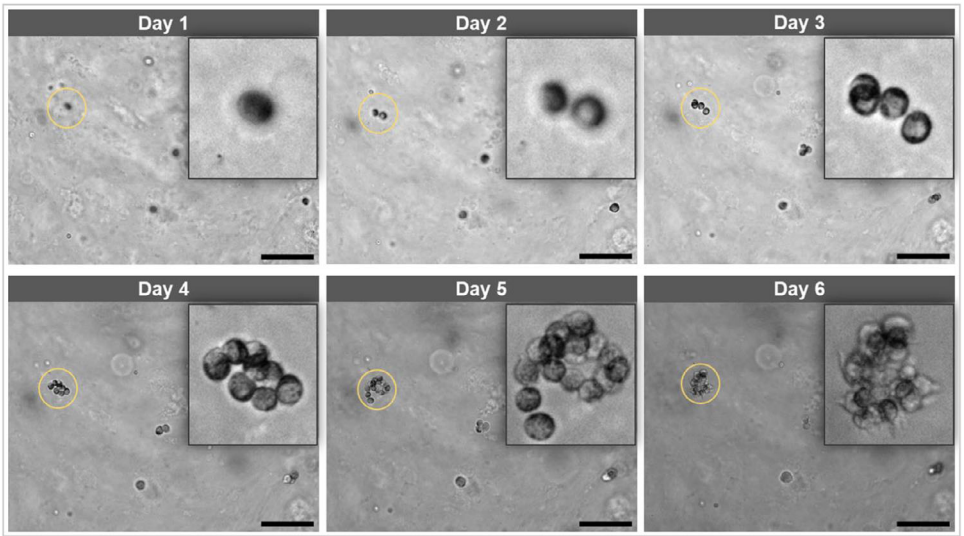

FIGURE 6 | Time-lapse bright-field images showing clonal growth of L929 cells encapsulated in BTP hydrogels (1.5 wt% fiber, 10 mol% CL) over 6 days. The yellow circles indicate the tracked colony, and the insets show magnified views of the same colony at each time point. Objective = 10 ×, scale bars = 100 μm. For time-lapse video, see Video S2. The colony growth dynamics were observed for other cell lines, including MCF-7, MDA-MB-231, and MDCK (Figures S15–S17 and Videos S3–S5).

in biological contexts. Furthermore, we encapsulated the cells based on SPAAC click chemistry, which may limit further cell aggregation by spatial confinement around the embedded cells during gelation.

Notably, despite its chemical and biological inertness and limited molecular dynamics, our hydrogel system still supports long-term (10-day) viability and enables cells to form expanding colonies as described above. To assess the origin of colony growth, we continuously acquired z-stack bright-field images of L929 cells encapsulated in hydrogels containing 1.5 wt.% fiber and 10 mol% CL over a time period of 10 days. In the initial images taken immediately after gelation, cells remained monodisperse throughout the gel (Video S1). Some cells appear as doublets likely originating from incomplete separation during cell passage. Therefore, initial cell aggregation during the gelation phase can be excluded as the origin of colony formation in our BTP system. This behavior distinguishes SPAAC-based crosslinked BTP hydrogels from previously reported synthetic supramolecular systems, where dynamic exchange or bioactive functionalization was required to sustain long-term 3D culture.

To investigate the growth pathway of multicellular assemblies in BTP hydrogels, we tracked cell behavior in hydrogels with 1.5 wt% fiber and 10 mol% CL over 10 days by live cell microscopy. Multicellular structures predominantly originated from clonal expansion of single cells (Figure 6; Video S2) or division of initial doublets/triplets (Figures S15–S17 and Videos S3–S5), rather than from cell aggregation. Moreover, occasional outliers in the measured live-event area (Figure 5) were attributable to the merging of two or more neighboring colonies (Figure S18 and Video S6). Even though this is not the primary focus of this work, our observations suggest that the matrix locally permits sufficient mechanical space and flexibility for single cells to undergo multiple divisions to form colonies even in the absence of adhesion ligands. Compared with other bioinert systems relying on pre-formed voids in gels or dynamic exchange mechanism, our findings underscore a key insight for designing synthetic microenvironments.

3 | Conclusion

In conclusion, we demonstrate that supramolecular polymer brushes, crosslinked via SPAAC chemistry in the presence of cells, provide a bio-orthogonal route to fabricate viscoelastic, shear-thinning, and bioinert hydrogels suitable for homogeneous 3D cell encapsulation. Our approach connects pre-assembled supramolecular bottlebrush fibers and creates robust hydrogels as cell scaffolds without compromising biocompatibility or the inherent noncovalent nature of the fibers. The mechanical properties of these hydrogels can be tuned by adjusting fiber concentration and the density of crosslinking connections. Across multiple cell lines, cell viability and growth were strongly dependent on fiber concentration: lower fiber contents promoted higher viability and clonal colony expansion over 10 days of culture. Remarkably, long-term survival and proliferation occurred for all tested cell lines in the absence of bioactive cues, highlighting that the fibrous microarchitecture and mechanical compliance of the matrix alone can sustain multicellular organization. Compared to previously reported fibrous hydrogels, the SPAAC-stabilized BTP system is based on predefined, non-dynamic fibers that remain structurally stable yet mechanically flexible, restricting cell migration while enabling local cellular organization and distinct clonal growth behavior. The nature of the polymer bottlebrush fibers, with their dense PEO shell and robust non-dynamic assembly, further opens an interesting avenue for designing complex structures that not only allow long-term studies but also enable integration of variable and even bulky biological cues. Our current system, characterized by its extended structural integrity, is therefore particularly suited for applications such as high-throughput drug screening or fundamental 3D cell-behavior studies, rather than for dynamic systems intended for rapid cell retrieval. Future investigations will focus on incorporating

such cues and biodegradable motifs to promote cell adhesion and matrix remodeling, as well as analyzing how local stiffness heterogeneity influences cell–cell and cell–matrix interactions.

4 | Experimental Section

If it is not stated differently, all solvents and reagents were commercially purchased from Sigma–Aldrich and used without further purification.

4.1 | Preparation of Supramolecular Fibers and Hydrogels

An overview of sample formulations for rheological investigations and 3D cell culture studies can be found in Table S1. Supramolecular fibers were prepared by the solvent switch method. Predetermined amounts of BTP and BTP-N_3 were added in 20 mL vial with a wide neck. Then, EtOH was added, and sonication was applied until the system was completely dissolved. Afterward, the mixture was stirred with a magnetic stirrer for 30 min at rt. After a complete dissolution of the system, Earle's balanced salt solution (EBBS) buffer was added at a speed of 1 mL h^{-1} via a syringe pump. Finally, the cap was removed to let a complete EtOH evaporation at rt. Afterward, predetermined amount of dibenzocyclooctyne-PEG_{10kDa}-dibenzocyclooctyne (crosslinker, CL) solution was added into the fiber solution by aiming the final fiber concentration. The system was incubated for 40 min at 37°C for complete gelation.

4.2 | Rheological Investigations

The samples for the rheological investigation were prepared by strictly following the fiber and gel preparation protocols. The rheological properties of the samples were investigated using a KINEXUS Prime lab+ rheometer (NETZSCH) equipped with a Peltier-Plate Cartridge and Active Hood (temperature range: −5°C–180°C). All measurements were performed by keeping a constant temperature at 37°C. To prevent sample dehydration, a saturated atmosphere was created inside the Active Hood by adding water.

4.2.1 | Sample Preparation

For each measurement, the fiber solution and the crosslinker solution were rapidly mixed by a pipette and immediately dispensed onto the measuring plate with a pre-equilibrated temperature at 37°C. A 25 mm stainless steel cone-plate geometry with a smooth surface was used for all measurements. The cone angle was 1° with a defined working gap of 0.027 mm as specified in the instrument configuration. Any excess liquid was carefully removed.

4.2.2 | Amplitude Sweep

To determine the linear viscoelastic range, amplitude sweep tests were performed. The complex shear strain was varied from 0.1% to 100% at a constant frequency of 1 Hz. Storage modulus (G′) and loss modulus (G″) were recorded as a function of strain, and the linear viscoelastic (LVE) range was defined for subsequent measurements.

4.2.3 | Frequency Sweep

Frequency sweep tests were conducted in the range from 0.1 to 100 Hz, with the complex shear strain fixed at 0.5%, which was within the previously determined linear viscoelastic range. G′ and G″ were measured as a function of frequency. All frequency sweep measurements were performed in triplicate to ensure reproducibility.

4.2.4 | Gelation Time

To determine the gelation time, time-dependent measurements (time sweeps) were performed at a constant frequency of 1 Hz and a complex shear strain of 0.5%, both within the linear viscoelastic range as previously established. The evolution of G′ and G″ was monitored over time to analyze the kinetics of gel formation.

4.2.5 | Relaxation Measurement

Using the same geometry as previously established, relaxation measurements were conducted with a constant strain of 3%. The change in shear stress was recorded over a period of 10 min. Afterward, the data were normalized on a scale of 1-0 AU (arbitrary units), using the maximum value of the shear stress as the starting point for the relaxation measurement. This allowed for a graphical evaluation of the half-life at a shear stress normalized to 0.5 AU. All measurements were conducted with at least four replicates ($n = 4$) to ensure reproducibility.

4.2.6 | Step-Strain Experiments

Recovery of the hydrogels was investigated by monitoring the shear modulus as a function of time after subjecting the gels to a severe shear deformation of 200% strain for 1 min during the designated shearing phase. This shearing period was followed by a recovery phase, where a minor strain of 0.5% was applied. All measurements were performed at a frequency of 1 Hz. This entire cycle, comprising of a shearing and recovery phase, was consecutively executed five times on the same sample to assess repeatability and recovery behavior.

4.2.7 | Sample Preparation and Hydrogel Swelling Measurement

Hydrogels with a fiber content of 1.2–2.5 wt% were prepared in a 1.5 mL Eppendorf vial, each with a volume of 150 µL, as previously described. After incubation at 37°C for 4 h to enable complete gelation, the initial weight was noted, and 1 mL of Milli-Q water was added to each gel for swelling. After each subsequent incubation period on days 1, 3, 7, and 10, excess and

condensed water were carefully removed, and the weight changes were recorded. Following each recording, the swelling process was reset with the addition of another 1 mL Milli-Q water to the same gel sample for the next incubation period. This process was repeated for three replicates per each gel. After 10 days, additional measurements for frequency sweep, strain recovery, and shear stress relaxation were performed on these hydrogel samples.

4.3 | Determination of Fiber Content-Dependent Diffusion Coefficients by FRAP Experiments

A fluorescence recovery after photobleaching (FRAP) experiments were conducted for the fiber extremes of 1.2 and 2.5 wt% with 10 mol% CL to understand if the fiber content-related viability could be explained by the diffusion coefficients and mobility fractions. For this purpose, fluorescein labeled IgG (FITC-IgG) was added into the selected fiber formulations by aiming a final FITC-IgG concentration of 0.03 mM. Afterward, 50 µL of each hydrogel formulation was placed into the wells of ibidi, µ-Slide 15 Well 3D (ibidi GmbH, Germany). The wells were further sealed with an adhesive tape in order to avoid water evaporation and subjected to a confocal laser scanning microscope Zeiss LSM 880 mounted on an Axio Observer stative (Carl Zeiss, Oberkochen, Germany) equipped with an EC Plan−Neofluor 10 × /0.3 objective. First, images of the fresh hydrogels, as pre-bleached images, with xy dimensions of 850 µm × 850 µm, were captured with the 488 nm argon laser set to 2% power intensity. The incorporated dye (FITC) was detected with a 32 channels GaAsP detector using a filter−free adjustable prism optic to detect the desired wavelength range of λem FITC = 495 to 519 nm. Subsequently, a small area of 340 µm × 340 µm in xy direction was bleached using 100% power of the 488 nm laser for 317 s and an integration time of 177 µs pixel^{-1} with a scaling of 0.4 µm × 0.4 µm per pixel. After bleaching, the time-resolved recovery of fluorescence intensity in the bleached region was monitored every minute until no further increase in fluorescence signal intensity was observed by additionally peaking an unbleached area in the image as an internal fluorescence reference to obtain the mean fluorescence intensity and to track any presence of general photobleaching due to repeated measurement cycles. FRAP image sequences were analyzed with a custom MATLAB script (MATLAB R2022a) adopted from the implementation by Richbourg and Peppas [46] based on the model developed by Jönsson et al. [47]. An automated batch processing of TIFF image stacks was performed via the script by calculation mean fluorescence intensities for the bleached region over time. Recovery curves were fitted with one- and two-component diffusion models to determine apparent diffusion coefficients (D, µm^2 s^{-1}) represented as Fit 1 and 2, and the immobile fractions (γ_0, g0) (Figure S7).

4.4 | Biological Investigations

4.4.1 | Cell Culture

L929 and MDCK cell lines were purchased from CLS Cell Lines Service GmbH, Eppelheim, Germany. MCF-7 and MDA-MB-231 cell lines were obtained from Leibniz Institute DSMZ-German Collection of Microorganisms and Cell Cultures GmbH, Germany. All cell lines were cultured in TC treated cell culture flasks (Labsolute Th. Geyer GmbH & Co. KG) at 37°C under a humidified 5% (v/v) CO_2 atmosphere. For L929 cells, Dulbecco's modified Eagle medium (D10) (2 mM l-glutamine (Capricorn Scientific, Germany) supplemented with 10% fetal calf serum (FCS, Capricorn Scientific, Germany), 100 U mL^{-1} penicillin, and 100 µg mL^{-1} streptomycin (Capricorn Scientific, Germany) was used. MCF-7 and MDA-MB-231 cells were cultured with the addition of 1% MEM non-essential amino acids (Capricorn Scientific GmbH, Germany) to the D10 medium. For MDCK cells, Ham's F12 Medium (2 mM l-glutamine supplemented with 5% fetal calf serum, 100 U mL^{-1} penicillin, and 100 µg mL^{-1} streptomycin) was used for culturing. Dulbecco's phosphate-buffered saline (1x) (DPBS) and trypsin-EDTA (Capricorn Scientific GmbH, Germany) were used for each cell passaging. All 3D cell culture experiments were conducted with the internal passage numbers of 10 to 14 with > 97% viability.

4.4.2 | Live/Dead Cell Analysis by FDA/PI Staining

µ-Slide 15 Well 3D (ibidi GmbH, Germany) was used for 3D cell culture. 30 mg/mL fiber stock solution was prepared. Cells and CL solutions were added by aiming final fiber content of 1.2 to 2.5 wt%. For each well, 12 µL fiber/CL solution bearing 2000 cells was added. The slides were incubated at 37°C under a humidified 5% (v/v) CO_2 atmosphere for 40 min. After gelation was completed, cell type specific culture media was added on top of the gels, followed by culture for 2, 6, and 10 days. Every third day of culturing, the media exchange was performed. Each formulation was prepared as a triplicate. The viability of cells was examined microscopically using a fluorescein diacetate/ propidium iodide (FDA/PI) staining assay. For that, gels were submerged with medium containing PI (10 µg mL^{-1}) and FDA (10 µg mL^{-1}) and incubated for 20 min at 37°C. The green (FDA) and red (PI) fluorescence signals for live/dead cell analysis, as well as the transmitted light signals representing general morphology of cells in the gel, were captured by a CLSM Zeiss LSM 880 mounted on an Axio Observer stative (Carl Zeiss) equipped with an EC Plan−Neofluor 10 × /0.3 objective. For excitation of FDA and PI a 488 nm Argon laser and a 561 nm diode laser were used, respectively. Fluorescence emission was detected at 2% laser power for both 488 and 561 nm with a 32 channels GaAsP detector using a filter−free adjustable prism optic to detect the desired wavelength range of λem FDA = 493 to 596 nm and λem PI = 566 to 718 nm. A main beam path splitter at 488 and 561 nm was used in order to exclude excitation light from detection. Parallel to capturing fluorescence signals, the samples were imaged in transmission mode using identical laser power for the detection of laser light transmitted through the material. Colocalization was visualized in overlay images of the three channels. Images were acquired using ZEN 3.12 software (Carl Zeiss Microscopy GmbH, Germany).

4.4.3 | Time-Lapse Imaging of Multicellular Aggregate Formation by Live Cell Microscopy

To continuously monitor the growth and morphology of different cell types in BTP hydrogel (1.5 wt% fober and 10 mol% CL) under optimal conditions, a live-cell incubation unit (BioSpa,

BioTek Instruments, Agilent Technologies) in combination with an automated microscopy station (Cytation 5, BioTek Instruments, Agilent Technologies) was utilized. For this purpose, a non-treated 96-well plate with a flat bottom (Greiner Bio-One GmbH, Germany) was used. The samples for each cell line were prepared by aiming 8000 cells embedded in 40 µL hydrogel and submerged with 60 µL of the required cell culture media. Incubation was performed at 37°C in the BioSpa unit with a humidified atmosphere containing 5% CO_2. Every 3 h, the plate was automatically transferred to the live cell microscope set to the same culture conditions as presented in the BioSpa. In each well, a specific spot, which was predefined by user set beacons, was imaged in bright field mode with automated exposure settings and an autofocus based on the size of the 10 × objective (Olympus UPLFLN). In total, a z-stack of 49 optical slices with a step size of 10 µm was aimed, resulting in an observed sample thickness of 480 µm. After the completion of each imaging process, the plate was automatically relocated to the BioSpa incubator and kept there until the next cycle. All over, image data of 80 timepoints during the 10 days of culture were collected. Nevertheless, only representative images of day 0 to 6 were used to obtain time-lapse sequences of specific cell spots to demonstrate individual colony growth characteristics. To generate videos from selected images, raw microscopy data were first processed through ImageJ software, version 1.54p (National Institutes of Health, USA) to correct misalignment in the images caused by shifts in culture plate position during automated transfer. The resulting videos were further cropped, annotated, and compiled for a better presentation by utilizing general-purpose video editing software.

4.4.4 | Image Analysis by Deep-Learning

Image segmentation and analysis on raw image data were performed using the pre-trained deep learning model, Segment Anything Model 2.1 (SAM2.1, Meta AI), specifically the large model variant (sam2_hiera_large.pt, 224.4 M parameters) [41]. The model was implemented in Python programming language and deployed on a Mac mini M4 Pro equipped with a 20-core GPU and 64GB of RAM, leveraging Apple Silicon's Scalable Matrix Extension (SME) for optimized matrix operations. SAM2.1 was configured to run on the Metal Performance Shaders (MPS) backend to maximize computational efficiency. Post-segmentation analysis was conducted using the OpenCV library [42], which facilitated mask annotation and visualization of segmented microscopy images. For the quantitative analysis, outlier cells and colonies were not included.

4.4.5 | Statistical Analysis

All statistical analyses were performed in R (version 4.5.1) using the packages dplyr, ggplot2, rstatix, and tidyr. Data normality for each condition was assessed using the Shapiro–Wilk test. For non-normally distributed data, differences among incubation days within the same fiber content were evaluated using the Kruskal–Wallis test, followed by pairwise Wilcoxon rank-sum tests with Bonferroni-adjusted p-values. For comparisons between fiber contents within the same incubation day, data were first tested for normality in each group. If both groups were normally distributed, equality of variances was examined using an F-test; depending on the result, either Student's t-test (equal variances) or Welch's t-test (unequal variances) was applied. If at least one group was non-normal, the Mann–Whitney U-test was used. Significance levels were denoted as follows: $p < 0.05$ (*), $p < 0.01$ (**), $p < 0.001$ (***). Median values for each group were calculated for descriptive reporting. All boxplots display individual data points, median values, and standard deviation whiskers by utilizing OriginPro2022b software.

Acknowledgements

The authors thank Boehringer Ingelheim Foundation (BIS) for funding this project as part of an Exploration Grant. The German Science Foundation (DFG) is further acknowledged for support within the Emmy-Noether Programme (Project-ID: 358263073), the Heisenberg-Programme (Project-ID: 517761335), and the Collaborative Research Centre PolyTarget (Project-ID: 316213987 – SFB 1278). The authors are thankful to Sandra Opel for the preparation of unmodified benzenetrispeptides motifs. The authors are grateful to Hans F. Ulrich and Sebastian Städter for fruitful discussions on BTP-based supramolecular system. The authors acknowledge Sandra Henk and Carolin Kellner for maintaining the cell lines, and Elisabeth Moek for the assistance in mycoplasma detection testing. The authors thank Hüseyin Tarik Cetin for correcting the alignment of live-cell images, which are then compiled into videos.

Open access funding enabled and organized by Projekt DEAL.

Conflicts of Interest

The authors declare no conflict of interest.

Data Availability Statement

The data that support the findings of this study are available from the corresponding author upon reasonable request.

References

1. L. Rijns, M. G. T. A. Rutten, A. F. Vrehen, A. A. Aldana, M. B. Baker, and P. Y. W. Dankers, "Mimicking the Extracellular World: From Natural to Fully Synthetic Matrices Utilizing Supramolecular Biomaterials," *Nanoscale* 16 (2024): 16290–16312.

2. P. Lu, D. Ruan, M. Huang, et al., "Harnessing the Potential of Hydrogels for Advanced Therapeutic Applications: Current Achievements and Future Directions," *Signal Transduction and Targeted Therapy* 9 (2024): 166.

3. J. Nicolas, S. Magli, L. Rabbachin, S. Sampaolesi, F. Nicotra, and L. Russo, "3D Extracellular Matrix Mimics: Fundamental Concepts and Role of Materials Chemistry to Influence Stem Cell Fate," *Biomacromolecules* 21 (2020): 1968–1994.

4. P. Bertsch, M. Diba, D. J. Mooney, and S. C. G. Leeuwenburgh, "Self-Healing Injectable Hydrogels for Tissue Regeneration," *Chemical Reviews* 123 (2023): 834–873.

5. S. Correa, A. K. Grosskopf, H. L. Hernandez, et al., "Translational Applications of Hydrogels," *Chemical Reviews* 121 (2021): 11385–11457.

6. E. A. Aisenbrey and W. L. Murphy, "Synthetic Alternatives to Matrigel," *Nature Reviews Materials* 5 (2020): 539–551.

7. A. H. Isaac, S. Y. Recalde Phillips, E. Ruben, et al., "Impact of PEG Sensitization on the Efficacy of PEG Hydrogel-Mediated Tissue Engineering," *Nature Communications* 15 (2024): 3283.

8. A. S. Wadajkar, B. Koppolu, M. Rahimi, and K. T. Nguyen, "Cytotoxic Evaluation of N-isopropylacrylamide Monomers and Temperature-

Sensitive poly(N-isopropylacrylamide) Nanoparticles," *Journal of Nanoparticle Research* 11 (2009): 1375–1382.

9. A. Naba, "Mechanisms of Assembly and Remodelling of the Extracellular Matrix," *Nature Reviews Molecular Cell Biology* 25 (2024): 865–885.

10. T. E. Sutherland, D. P. Dyer, and J. E. Allen, "The Extracellular Matrix and The Immune System: A Mutually Dependent Relationship," *Science* 379 (2023): abp8964.

11. J. L. Chitty and T. R. Cox, "The Extracellular Matrix in Cancer: From Understanding to Targeting," *Trends in Cancer* 11 (2025): 839–849, https://doi.org/10.1016/j.trecan.2025.05.003.

12. L. Zhang, J. Zhou, and W. Kong, "Extracellular Matrix in Vascular Homeostasis and Disease," *Nature Reviews Cardiology* 22 (2025): 333–353.

13. L. Li, S. Wang, Y. Chen, et al., "Hydrogels Mimicking the Viscoelasticity of Extracellular Matrix for Regenerative Medicine: Design, Application, and Molecular Mechanism," *Chemical Engineering Journal* 498 (2024): 155206.

14. M. Rizwan, A. E. G. Baker, and M. S. Shoichet, "Designing Hydrogels for 3D Cell Culture Using Dynamic Covalent Crosslinking," *Advanced Healthcare Materials* 10: 2100234.

15. C. Fan and D.-A. Wang, "Macroporous Hydrogel Scaffolds for Three-Dimensional Cell Culture and Tissue Engineering," *Tissue Engineering Part B: Reviews* 23 (2017): 451.

16. L. Rijns, M. B. Baker, and P. Y. W. Dankers, "Using Chemistry To Recreate the Complexity of the Extracellular Matrix: Guidelines for Supramolecular Hydrogel–Cell Interactions," *Journal of the American Chemical Society* 146 (2024): 17539–17558.

17. R. Eelkema and A. Pich, "Pros and Cons: Supramolecular or Macromolecular: What Is Best for Functional Hydrogels with Advanced Properties?," *Advanced Materials* 32 (2020): 1906012.

18. M. J. Webber, E. A. Appel, E. W. Meijer, and R. Langer, "Supramolecular Biomaterials," *Nature Materials* 15 (2016): 13–26.

19. S. R. Caliari and J. A. Burdick, "A Practical Guide to Hydrogels for Cell Culture," *Nature Methods* 13 (2016): 405–414.

20. T. Klein, H. F. Ulrich, F. V. Gruschwitz, et al., "Impact of Amino Acids on the Aqueous Self-Assembly of Benzenetrispeptides into Supramolecular Polymer Bottlebrushes," *Polymer Chemistry* 11 (2020): 6763–6771.

21. T. Klein, H. F. Ulrich, F. V. Gruschwitz, et al., "Overcoming the Necessity of a Lateral Aggregation in the Formation of Supramolecular Polymer Bottlebrushes in Water," *Macromolecular Rapid Communications* 42 (2021): 2000585.

22. F. V. Gruschwitz, T. Klein, M. T. Kuchenbrod, et al., "Kinetically Controlling the Length of Self-Assembled Polymer Nanofibers Formed by Intermolecular Hydrogen Bonds," *ACS Macro Letters* 10 (2021): 837–843.

23. F. V. Gruschwitz, F. Hausig, P. Schüler, et al., "Shear-Thinning and Rapidly Recovering Hydrogels of Polymeric Nanofibers Formed by Supramolecular Self-Assembly," *Chemistry of Materials* 34 (2022): 2206–2217.

24. H. F. Ulrich, C. C. Pihlamagi, T. Klein, C. Bakkali-Hassani, S. Catrouillet, and J. C. Brendel, "Injectable Biocompatible Hydrogels with Tunable Strength Based on Crosslinked Supramolecular Polymer Nanofibers," *Journal of Materials Chemistry B* 13 (2025): 2003–2014.

25. N. J. Agard, J. A. Prescher, and C. R. Bertozzi, "A Strain-Promoted [3 + 2] Azide–Alkyne Cycloaddition for Covalent Modification of Biomolecules in Living Systems," *Journal of the American Chemical Society* 126 (2004): 15046–15047.

26. M. R. Arkenberg, H. D. Nguyen, and C.-C. Lin, "Recent Advances in Bio-Orthogonal and Dynamic Crosslinking of Biomimetic Hydrogels," *Journal of Materials Chemistry B* 8 (2020): 7835–7855.

27. S. Hafeez, M. C. Decarli, A. Aldana, et al., "In Situ Covalent Reinforcement of a Benzene-1,3,5-Tricarboxamide Supramolecular Polymer Enables Biomimetic, Tough, and Fibrous Hydrogels and Bioinks," *Advanced Materials* 35 (2023): 2301242.

28. J. Thomas, N. Gupta, J. P. Joseph, V. Chopra, A. Pal, and D. Ghosh, "Mechanical Integrity in a Dynamic Interpenetrating Hydrogel Network of Supramolecular Peptide–Polysaccharide Supports Enhanced Chondrogenesis," *ACS Biomaterials Science & Engineering* 7 (2021): 5798–5809.

29. L. G. Brunel, C. M. Long, F. Christakopoulos, et al., "Reinforcement of Fibrillar Collagen Hydrogels with Bioorthogonal Covalent Crosslinks," *Biomacromolecules* 26 (2025): 4404–4418.

30. L. G. Brunel, C. M. Long, F. Christakopoulos, et al., "Interpenetrating Networks of Fibrillar and Amorphous Collagen Promote Cell Spreading and Hydrogel Stability," *Acta Biomaterialia* 193 (2025): 128–142.

31. S. Hafeez, F. R. Passanha, A. J. Feliciano, et al., "Modular Mixing of Benzene-1,3,5-tricarboxamide Supramolecular Hydrogelators Allows Tunable Biomimetic Hydrogels for Control of Cell Aggregation in 3D," *Biomaterials Science* 10 (2022): 4740–4755.

32. L. Rijns, H. Duijs, R. P. M. Lafleur, et al., "Molecularly Engineered Supramolecular Thermoresponsive Hydrogels with Tunable Mechanical and Dynamic Properties," *Biomacromolecules* 25 (2024): 4686–4696.

33. M. Diba, S. Spaans, S. I. S. Hendrikse, et al., "Engineering the Dynamics of Cell Adhesion Cues in Supramolecular Hydrogels for Facile Control Over Cell Encapsulation and Behavior," *Advanced Materials* 33 (2021): 2008111.

34. P. Yang, G. Boer, F. Snow, et al., "Test and Tune: Evaluating, Adjusting and Optimising the Stiffness of Hydrogels to Influence Cell Fate," *Chemical Engineering Journal* 505 (2025): 159295.

35. A. J. Berger, K. M. Linsmeier, P. K. Kreeger, and K. S. Masters, "Decoupling the Effects of Stiffness and Fiber Density on Cellular Behaviors via an Interpenetrating Network of Gelatin-Methacrylate and Collagen," *Biomaterials* 141 (2017): 125–135.

36. D. C. Schoenmakers, A. E. Rowan, and P. H. J. Kouwer, "Crosslinking of Fibrous Hydrogels," *Nature Communications* 9 (2018): 2172.

37. C. M. Madl, L. M. Katz, and S. C. Heilshorn, "Bio-Orthogonally Crosslinked, Engineered Protein Hydrogels with Tunable Mechanics and Biochemistry for Cell Encapsulation," *Advanced Functional Materials* 26 (2016): 3612–3620.

38. J. Zheng, L. A. Smith Callahan, J. Hao, et al., "Strain-Promoted Cross-Linking of PEG-Based Hydrogels via Copper-Free Cycloaddition," *ACS Macro Letters* 1 (2012): 1071–1073.

39. H. Zhan, H. de Jong, and D. W. P. M. Löwik, "Comparison of Bioorthogonally Cross-Linked Hydrogels for In Situ Cell Encapsulation," *ACS Applied Bio Materials* 2 (2019): 2862–2871.

40. M. Pires Figueiredo, S. Rodríguez-Fernández, F. Copes, and D. Mantovani, "Review of Collagen Type I-Based Hydrogels: Focus on Composition-Structure-Properties Relationships," *npj Biomedical Innovations* 2 (2025): 16.

41. A. Kirillov, E. Mintun, N. Ravi, et al., in *Proceedings of the IEEE/CVF International Conference on Computer Vision* (Computer Vision Foundation (CVF), 2023).

42. G. Bradski, "The OpenCV Library," *Dr Dobb's Journal of Software Tools* 25 (2000): 120–123.

43. P. Blázquez-Carmona, R. Ruiz-Mateos, J. Barrasa-Fano, et al., "Quantitative Atlas of Collagen Hydrogels Reveals Mesenchymal Cancer Cell Traction Adaptation to the Matrix Nanoarchitecture," *Acta Biomaterialia* 185 (2024): 281–295.

44. N. Schierbaum, J. Rheinlaender, and T. E. Schäffer, "Viscoelastic Properties of Normal and Cancerous Human Breast Cells are Affected Differently by Contact to Adjacent Cells," *Acta Biomaterialia* 55 (2017): 239–248.

45. Y. Zhou, J. Li, Y. Zhang, et al., "Establishment of a Physical Model for Solute Diffusion in Hydrogel: Understanding the Diffusion of Proteins in Poly(sulfobetaine methacrylate) Hydrogel," *The Journal of Physical Chemistry B* 121 (2017): 800–814.

46. N. R. Richbourg and N. A. Peppas, "High-Throughput FRAP Analysis of Solute Diffusion in Hydrogels," *Macromolecules* 54 (2021): 10477–10486.

47. P. Jönsson, M. P. Jonsson, J. O. Tegenfeldt, and F. Höök, "A Method Improving the Accuracy of Fluorescence Recovery After Photobleaching Analysis," *Biophysical Journal* 95 (2008): 5334–5348.

48. C. M. Kasse, A. C. Yu, A. E. Powell, et al., "Subcutaneous Delivery of an Antibody Against SARS-CoV-2 From a Supramolecular Hydrogel Depot," *Biomaterials Science* 11 (2023): 2065–2079.

49. M. H. Hettiaratchi, A. Schudel, T. Rouse, et al., "A Rapid Method for Determining Protein Diffusion Through Hydrogels for Regenerative Medicine Applications," *APL Bioengineering* 2 (2018): 026110.

50. C. N. Salinas and K. S. Anseth, "The Influence of the RGD Peptide Motif and its Contextual Presentation in PEG Gels on Human Mesenchymal Stem Cell Viability," *Journal of Tissue Engineering and Regenerative Medicine* 2 (2008): 296.

51. D. MacPherson, Y. Bram, J. Park, and R. E. Schwartz, "Peptide-Based Scaffolds for the Culture and Maintenance of Primary Human Hepatocytes," *Scientific Reports* 11 (2021): 6772.

52. V. I. B. Castro, A. R. Araújo, F. Duarte, et al., "Glycopeptide-Based Supramolecular Hydrogels Induce Differentiation of Adipose Stem Cells Into Neural Lineages," *ACS Applied Materials & Interfaces* 15 (2023): 29998–30007.

53. J. J. Panda, R. Dua, A. Mishra, B. Mittra, and V. S. Chauhan, "3D Cell Growth and Proliferation on a RGD Functionalized Nanofibrillar Hydrogel Based on a Conformationally Restricted Residue Containing Dipeptide," *ACS Applied Materials & Interfaces* 2 (2010): 2839–2848.

54. O. Chaudhuri and D. J. Mooney, "Anchoring Cell-Fate Cues," *Nature Materials* 11 (2012): 568–569.

55. Y.-H. Peng, S.-K. Hsiao, K. Gupta, et al., "Dynamic Matrices with DNA-Encoded Viscoelasticity for Cell and Organoid Culture," *Nature Nanotechnology* 18 (2023): 1463–1473.

56. M. Takeichi, "Cadherin Cell Adhesion Receptors as a Morphogenetic Regulator," *Science* 251 (1991): 1451–1455.

57. G. Mbalaviele, C. R. Dunstan, A. Sasaki, P. J. Williams, G. R. Mundy, and T. Yoneda, "E-Cadherin Expression in Human Breast Cancer Cells Suppresses the Development of Osteolytic Bone Metastases in an Experimental Metastasis Model," *Cancer Research* 56 (1996): 4063–4070.

58. S. Toda, L. R. Blauch, S. K. Y. Tang, L. Morsut, and W. A. Lim, "Programming Self-Organizing Multicellular Structures with Synthetic Cell-Cell Signaling," *Science* 361 (2018): 156–162.

59. B. Nzigou Mombo, B. M. Bijonowski, C. A. Raab, et al., "Reversible Photoregulation of Cell-Cell Adhesions with opto-E-cadherin," *Nature Communications* 14 (2023): 6292.

60. M. Gloerich, J. M. Bianchini, K. A. Siemers, D. J. Cohen, and W. J. Nelson, "Cell Division Orientation is Coupled to Cell–Cell Adhesion by the E-cadherin/LGN Complex," *Nature Communications* 8 (2017): 13996.

61. F. Pampaloni, E. G. Reynaud, and E. H. K. Stelzer, "The Third Dimension Bridges the Gap between Cell Culture and Live Tissue," *Nature Reviews Molecular Cell Biology* 8 (2007): 839–845.

62. L. M. Weber, K. N. Hayda, K. Haskins, and K. S. Anseth, "The Effects of Cell–Matrix Interactions on Encapsulated β-Cell Function Within Hydrogels Functionalized with Matrix-Derived Adhesive Peptides," *Biomaterials* 28 (2007): 3004–3011.

63. J. Zhu, "Bioactive Modification of Poly(ethylene glycol) Hydrogels for Tissue Engineering," *Biomaterials* 31 (2010): 4639–4656.

64. R. C. Ollier and M. J. Webber, "Mechanoresponsive Hydrogels Emerging from Dynamic and Non-Covalent Interactions," *Advanced Materials* 37 (2025): 2507397.

65. L. Rijns, J. W. Peeters, S. I. S. Hendrikse, et al., "Importance of Molecular and Bulk Dynamics in Supramolecular Hydrogels in Dictating Cellular Spreading," *Chemistry of Materials* 35 (2023): 8203–8217.

66. L. Rijns, M. J. Hagelaars, J. J. B. van der Tol, S. Loerakker, C. V. C. Bouten, and P. Y. W. Dankers, "The Importance of Effective Ligand Concentration to Direct Epithelial Cell Polarity in Dynamic Hydrogels," *Advanced Materials* 36 (2024): 2300873.

67. J. F. van Sprang, J. G. M. Aarts, M. G. T. A. Rutten, et al., "Co-Assembled Supramolecular Hydrogelators Enhance Glomerulogenesis in Kidney Organoids Through Cell-Adhesive Motifs," *Advanced Functional Materials* 34 (2024): 2404786.

68. H. F. Ulrich, T. Klein, Z. Zhao, et al., "Selective Activation of Dynamics in Kinetically Frozen Supramolecular Polymer Bottlebrush Assemblies," *Small* 21 (2025): 05481.

69. M. Rubinstein and A. N. Semenov, "Dynamics of Entangled Solutions of Associating Polymers," *Macromolecules* 34 (2001): 1058–1068.

70. X. Du, J. Zhou, J. Shi, and B. Xu, "Supramolecular Hydrogelators and Hydrogels: From Soft Matter to Molecular Biomaterials," *Chemical Reviews* 115 (2015): 13165–13307.

Supporting Information

Additional supporting information can be found online in the Supporting Information section.

Supporting File 1: adfm74006-sup-0001-SuppMat.docx.

Supporting File 2: adfm74006-sup-0002-VideoS1.wmv.

Supporting File 3: adfm74006-sup-0003-VideoS2.mp4.

Supporting File 4: adfm74006-sup-0004-VideoS3.mp4.

Supporting File 5: adfm74006-sup-0005-VideoS4.mp4.

Supporting File 6: adfm74006-sup-0006-VideoS5.mp4.

Supporting File 7: adfm74006-sup-0007-VideoS6.mp4.